

Source rupture model of the 2018 M_W 6.7 Iburi, Hokkaido earthquake from joint inversion of strong motion and InSAR observations

Chunmei Ren, Han Yue[✉], Teng Wang, and Zeyan Zhao

School of Earth and Space Sciences, Peking University, Beijing 100871, China

Corresponding author Yue H, email: yue.han@pku.edu.cn

Key points:

- Rupture model obtained using a joint inversion technique.
- Earthquake initiated in the upper mantle and ruptured into the lower-crust.
- Seismic slips may be promoted by low frictional strength introduced by high fluid pressure.

Abstract The 2018 M_W 6.7 Iburi earthquake shocked the eastern Iburi region to the west of the Hidaka Collision Zone in Hokkaido, which is a destructive inland earthquake. We resolved the kinematic rupture process of the event by combining strong motions (SM) and synthetic aperture radar (SAR) images in a joint inversion. The results reveal that the duration of the whole rupture is about 17s, yielding a total seismic moment of 1.4×10^{19} N·m ($M_W=6.7$). The main slip area is located at a depth of approximately 24 km with a peak slip of ~0.8m above the hypocenter. The comparison with the regional velocity model shows the earthquake was initiated in the upper mantle, while the majority of slips are located in the lower crust, which is an “aseismic” domain in the typical sandwich model. The location of the major slip area is consistent with a high-conductivity volume. We proposed a mechanism of low frictional property (<0.3) produced by high pore pressure to explain the abnormal high dip angle and centroid depth located in the ductile lower-crust. Aftershocks are distributed in areas where the Coulomb frictional stress increases due to co-seismic displacement with a mechanism conjugating to the mainshock.

Keywords: finite fault model; joint inversion; steep reversed earthquake.

Citation: Ren CM, Yue H, Wang T, and Zhao ZY (2021). Source rupture model of the 2018 M_W 6.7 Iburi, Hokkaido earthquake from joint inversion of strong motion and InSAR observations. *Earthq Sci* 34 (1): 88–101, doi: 10.29382/eqs-2020-0065.

Received 14 December 2020; received in revised form 1 February 2021; accepted 8 February 2021; available online 2 April 2021.

© The Seismological Society of China and Institute of Geophysics, China Earthquake Administration 2021.

1. Introduction

The Hokkaido area, situated at the conjunction of the Northeast Honshu Arc Trench and the Kuril Arc Trench systems, adjusts a complex tectonic process between Pacific (PA), North America (NA), and Eurasian (EU) plates. And the formation of the complicated tectonics in Hokkaido mainly attribute to two stages of collision (Arita et al., 1998; Sakakibara, 1986; Toyoshima, 1989). During the Paleogene, collision between the NA and EU plates with a right-lateral motion caused the amalgamation of the eastern Hidaka Metamorphic Belt and the western Poroshiri Ophiolite Complex Belt (Kimura, 1994). A wide area of deformation resulted by this interaction provides an arena for the following complex subduction and orogeny processes in the whole Hokkaido Island. Since the Late Miocene, the PA plate has been obliquely subducting along the Kuril Trench in south-west direction at a speed of 6–11 mm/a (Demets, 1992), uplifting the high-velocity Hidaka body thrust over the low-velocity crust (Moriya et al., 1998), and migrating the Kurile forearc sliver (KFS) westward to form the present foreland fold-and-thrust belt Hidaka collision zone (HCZ; Kimura, 1996). In addition to generating typical subduction zone earthquakes in a simple linear plate boundary, the ongoing collision between the EU plate and the KFS keep accumulating tectonic stress, and also producing active inland seismicity beneath the HCZ (Ito, 2002). This 2018 Hokkaido earthquake is located at the west margin of the HCZ, which may indicate

the inelastically response is transmitted over the HCZ and provides an opportunity to investigate the seismogenic scenario and mechanism around the HCZ area.

The 2018 $M_W 6.7$ Iburi, Hokkaido earthquake occurred on September 5, at 18:08 (UTC) was located near 42.69° N, 142.01° E with hypocenter depth at 37 km and focal mechanism solution with strike/dip/rake=358°/74°/113°, estimated by Japan Meteorological Agency (JMA). The maximum shaking intensity reached level VII for the first time in this area, which caused more than 6000 landslides, about 2000 houses destroyed and 40 lives lost. The subducted PA plate locates at 75–100 km depth beneath the source area (Hayes et al., 2012; Liu X et al., 2013;

Shiina et al., 2018), which is well below the centroid depth at 24 km, and the thickness of the crust in the epicentral area is about 32–34 km; thus this event is a typical intraplate event. Though catastrophic earthquakes are common in Hokkaido area, few moderate-to-large intraplate earthquakes occurred in the vicinity: there were no more than 10 events occurred beneath HCZ over the preceding century; and the latest two were the 1970 $M_6.7$ Hidaka earthquake with an estimated depth of 20–30 km and the 1982 $M_7.1$ Urakawa earthquake with an estimated depth of 18–35 km (Ichikawa, 1971; Moriya, 1972; Moriya et al., 1983) plotted in Figure 1, whose focal mechanisms are similar to the 2018 event but with more

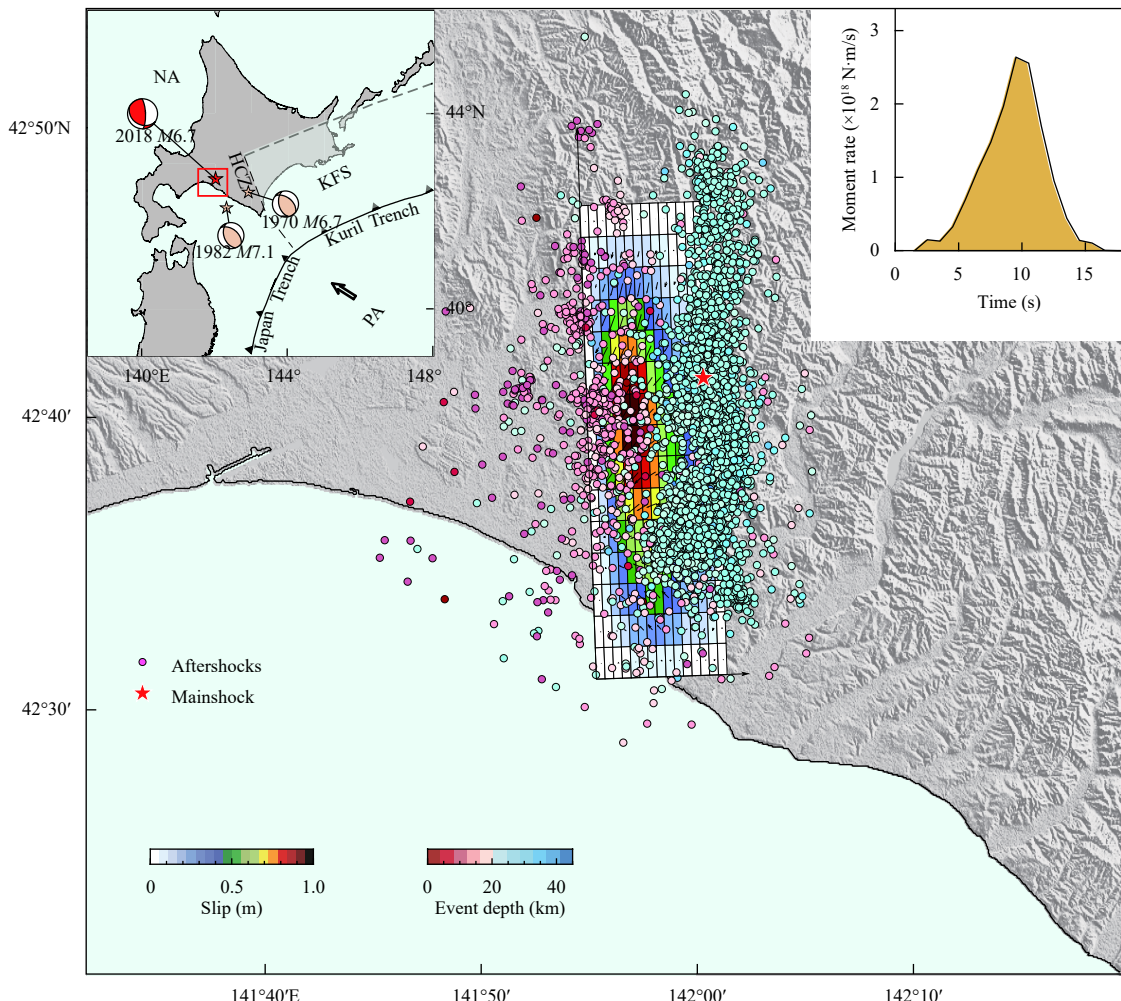


Figure 1. Tectonic setting, moment rate function, and finite fault model with aftershocks around. Regional tectonic setting is plotted in the inset map on the top-left. The red star marks the epicenter of the 2018 $M_W 6.7$ Iburi earthquake, whose focal mechanism is plotted as a red filled beach ball. And the pink stars mark the epicenters of the two historical analogous events, whose focal mechanism is plotted as pink filled beach ball. Red rectangle marks the plotting area of the main image. The arrow represents the relative motion between the Pacific Plate (PA) and the Northern America Plate (NA). A barbed line marks the Kuril Trench and the northern Japan Trench. The shaded area is the westward migrating Kurile forearc sliver (KFS) with the Hidaka collision zone (HCZ) located in the western boundary. In the main image, distribution of co-seismic slip is plotted in a white-red color scale. Aftershocks are plotted as dots with their hypocentral depths denoted as the filling colors. The epicenter of the mainshock is denoted as a red filled star. The moment rate function is plotted on the top-right.

flattish dip angles ($\sim 38^\circ$ – 44°) and shallower depths. The global CMT solution (www.globalcmt.org, Ekström et al., 2012) also reported a steep dip angle ($\sim 70^\circ$) for the 2018 Hokkaido earthquake, which is abnormally high for a reversed event since it is mechanically difficult to exist based on the principles of Anderson's faulting (Anderson, 1951) and is rarely observed on seismogenic faults. The intensive shaking, abnormal location and steep reverse angle of this event call for a detailed study of its rupture mechanisms. In addition, the source kinematic parameters can provide clues for seismic risk assessment and can also provide tectonic references for similar intraplate earthquakes.

The rupture process of the 2018 Hokkaido event has been investigated by different groups. Zang C et al. (2019) determined the focal mechanism (with strike/dip/rake as Np1: $144^\circ/22^\circ/64^\circ$; Np2: $352^\circ/70^\circ/100^\circ$) and centroid depth (26 km) of the event with inversion of teleseismic waveforms, revealing an upward rupture propagation, and proposed a seismogenic mechanism that cold brittle fore-arc crust caused by higher convergence rate of subduction and stress deviation in the crust enable deep and steep rupture occur. Katsumata et al. (2019) parameterized the fault plane with three segments following the trend of aftershocks and proposed the event started as a left-lateral strike-slip event on a stepover segment and then triggered ruptures on the main fault. Kobayashi et al. (2019b) constructed an east-dipping fault model with the geometry of $358^\circ/74^\circ/113^\circ$ (strike/dip/rake) by inverting interferometric SAR (InSAR) and Global Navigation Satellite System (GNSS) observations. They suggested that the static stress change due to the event can promote reverse fault slip on the southern part of the Ishikari-Teichi-Toen fault zone, which is located on the western side of the earthquake. Asano and Iwata (2019) used a fault model with three segments based on the aftershock distribution to inverted the rupture process from SM data, considering seismic wave propagation in a three-dimensional velocity structure. Their model shows the major slip is at depths of 20–30 km with a peak slip of 1.7 m. Kobayashi et al. (2019a) combined SM and GNSS data in their rupture process inversion and showed that the rupture initiated on a minor fault plane around the hypocenter and jump to the major fault plane 4–6 s after the initiation. The large slip also occurs at approximately 22 km depth. Guo ZL et al. (2019) determined the source parameters and fault slip distribution jointly using InSAR and GNSS datasets. They showed that the seismogenic fault is a blind NNW-trending (strike angle $\sim 347.2^\circ$), east-dipping (dip angle $\sim 79.6^\circ$) thrust fault, and the peak slip magnitude can approach 0.53 m at a depth of 15.5 km. Kubo et al. (2020) proposed a curved plane for the earthquake source and

simulated the overall ground-motion characteristics in the sedimentary layers.

Though different datasets were used to determine the rupture mechanism of the 2018 Hokkaido event, a joint inversion scheme combining seismic and geodetic observations are not adopted to determine the rupture process. Most recent earthquake studies demonstrated that joint inversion exploits complementary information in different datasets, yielding a more stable slip model (Yue H et al., 2020). In this study, we combine both SM and InSAR data in a joint inversion approach, attempt to validate the issue that whether fault plane expands as complicated as aftershocks' distribution and attempt to help to understand the initiation of the earthquake and its seismogenic mechanism.

2. Datasets and method

We selected three-component borehole acceleration waveforms from 17 KiK-net stations and ground acceleration waveforms from 6 K-net stations at epicentral distances within 100 km, ensuring good azimuth coverage (Figure 2a). We intercepted the first 60 seconds of the records and resampled them with an interval of 0.25 s after removing the mean value and linear trend. Original acceleration waveforms are integrated into velocity and applied with a filter with a frequency band from 0.01 Hz to 0.3 Hz to let each subfault meet the point source approximation condition (the wavelength is much larger than the scale of sub-fault). We accessed two pairs of SAR images of both ascending and descending tracks for SAR interference recorded by the Advanced Land Observing Satellite-2 (ALOS-2) from Japan Aerospace Exploration Agency (JAXA), which covers the main deformation area well (Figure 2b and 2c). Then we processed these data with the InSAR scientific computing environment software from the Jet Propulsion Laboratory (JPL)/California Institute of Technology (Caltech) (Rosen et al., 2012), unwrapped the interferograms through the Statistical-Cost Network-Flow Algorithm for Phase Unwrapping (SNAPHU) algorithm (Chen CW and Zebker, 2001) and down-sampled the unwrapped interferograms using a quadtree algorithm (Jónsson et al., 2002). The ascending image shows a maximum uplift of 10 cm and a subsidence of 5 cm in the line of sight (LOS) direction (Figure 2b), while the descending image shows about 15 cm uplift and 3 cm subsidence (Figure 2c), respectively. We adopted frequency-wavenumber integration methods to calculate Green's functions for geodetic data and seismic data, separately (Wang RJ et al., 2006; Zhu LP and Rivera, 2002). Two local velocity models were used to construct the one-dimensional velocity structures beneath each SM

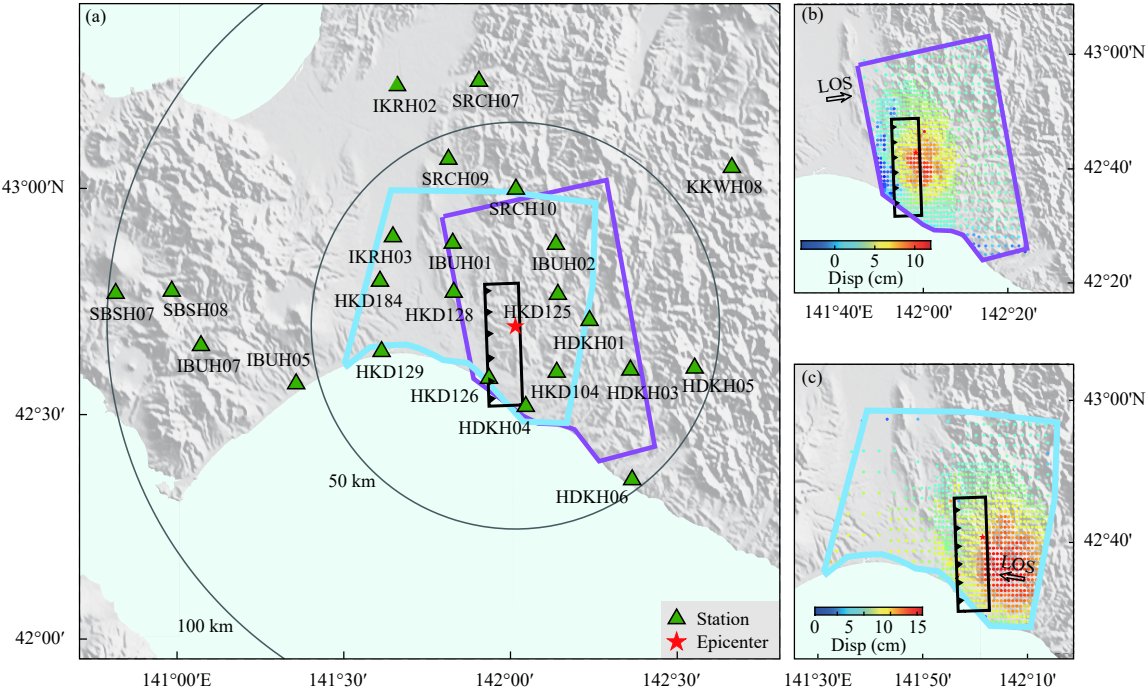


Figure 2. Data distribution. (a) The fault plane is plotted as a black rectangle with its top marked as the barbed edge. Strong-motion station used in rupture process inversion are plotted as green filled triangles. Areas covered by ascending and descend SAR orbits are denoted as magenta and cyan boxes, respectively. Ground displacements downsampled from un-wrapped SAR images for the ascending (b) and descending (c) orbits are in the top and bottom panels, respectively. Displacement samples are plotted as colored dots with the displacement amplitude denoted by their filling color. Fault plane and epicenter use the same symbol as Figure 2a.

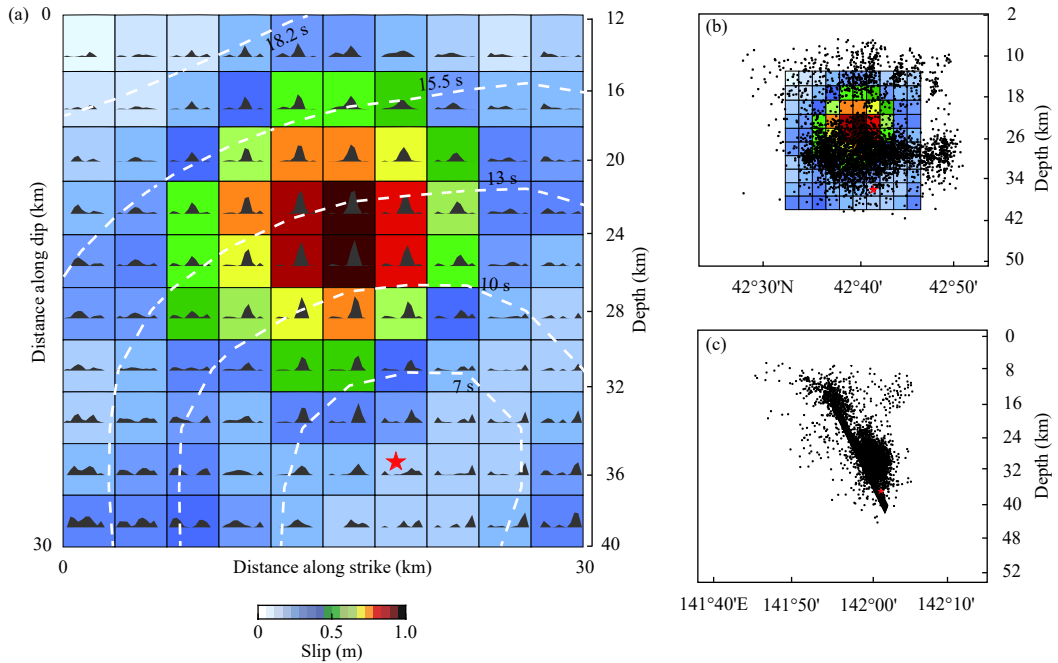


Figure 3. Slip distribution. (a) Slip distribution of the 2018 M_W 6.7 Iburi earthquake are plotted as a white-red color scale. The moment rate functions of each subfault are plotted as black filled curves in each patch. Hypocenter location is marked as a red-filled star and the rupture fronts are shaped as white curves with centroid time labeled aside. Relative location between co-seismic slips and aftershocks are plotted in the front (b) and side view (c) in the top and bottom panels respectively. Aftershocks are denoted as black dots in both images.

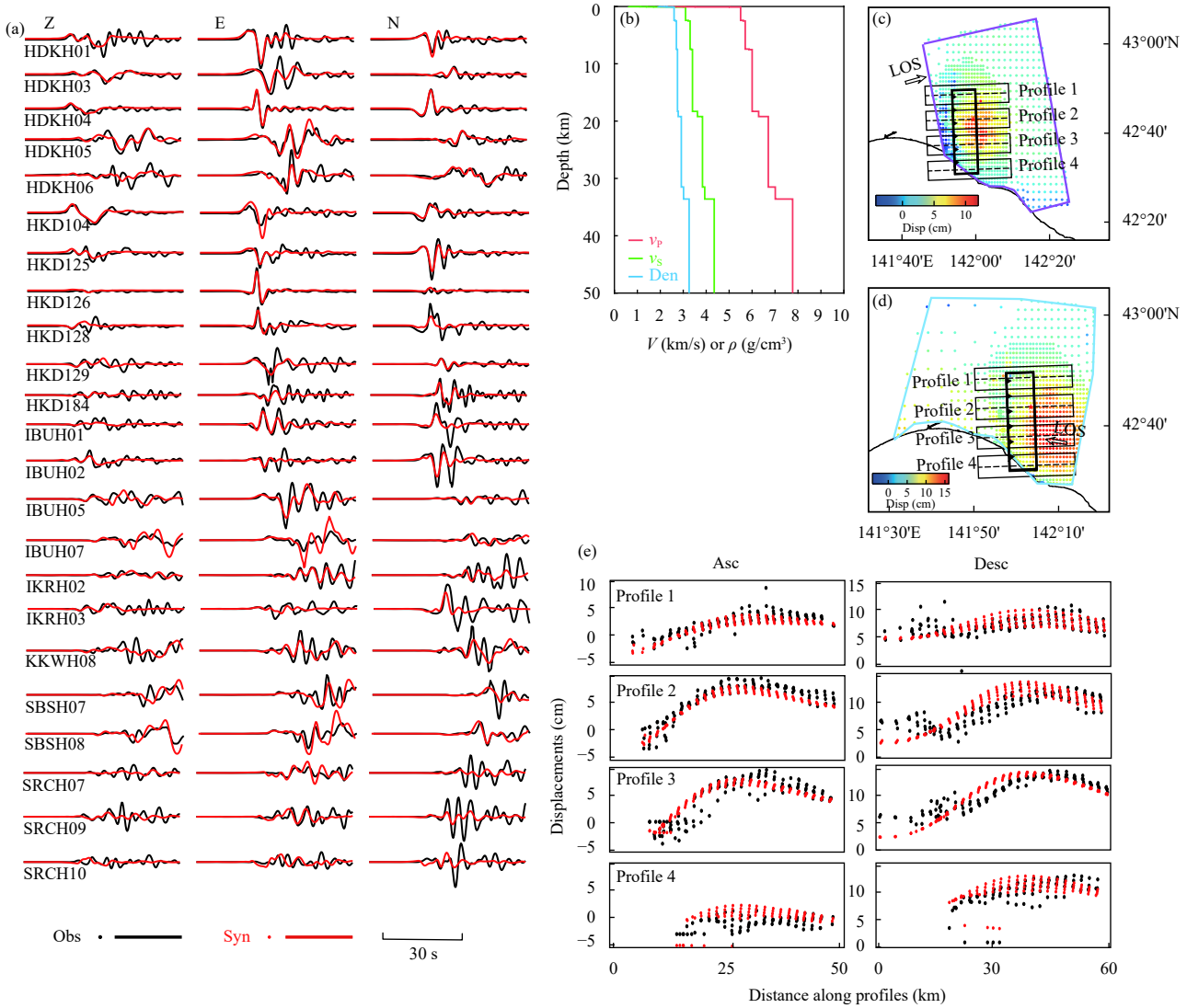


Figure 4. Data fitting. (a) Waveforms fitting to strong motion observations are plotted as black and red curves for observed and synthetic waveforms, respectively. The Z, E and N represent the three components of each station. (b) v_p , v_s and density of velocity structure are plotted as red, green and blue curves. (c) and (d), the same as figure 2b and figure 2c, except locations of four profiles are labeled. (e) Observed and fitted ground displacements are plotted as black and red dots along 4 profiles in each row, respectively. Displacements from the ascending and descending orbits are plotted in the left and right column, respectively.

station (Figure S1): the shallower part (<5 km) is extracted from Japan Integrated Velocity Structure Model (JIVSM) download from Japan Seismic Hazard Information Station(J-SHIS) (Koketsu et al., 2012) and the deeper portion (>5 km) is interpolated from a three-dimensional tomographic model for the southern Kuril arc (Liu X et al., 2013).

We parameterize the fault plane with respect to the mainshock focal mechanism reported by the JMA. The nodal plane was selected following the eastward dipping of the aftershock distribution. We also tested other strike and dip angles from 342° to 366° and 60° to 80° separately (Figure S2), taking into account that the different results gave different fault geometries (Table S1). For this M_W 6.7

earthquake, we parameterized it with a $30\text{ km} \times 30\text{ km}$ fault plane (Wells and Coppersmith, 1994). The fault plane is parameterized with ten subfaults along strike and dip directions, respectively; thus, the subfault size is uniformly $3\text{ km} \times 3\text{ km}$. The models of segmented or curved planes published in the previous studies (Figures S3–S6) also have been tested in our inversion, though we did not find significant evidence supporting a more complicated fault geometry. In our final result, we prefer to use a single fault plane model to parameterize the fault plane, for which the reason will be explained in the results part. Meanwhile, we adopted a multi-time-window (MTW) parameterization method, which approximates the source time function with multiple triangles (Hartzell and Heaton, 1983) and

nonnegative linear least squares inversion (Lawson and Hanson, 1974) to deduce the rupture kinematics. For each sub-fault, we use six triangles to parameterize the source time function. Each triangle has a 2 s duration and is shifted by 1 s from the previous triangle. We invert for slips along with two directions at rake $\pm 45^\circ$ from the point source rake angle (113°), so that the real slip directions can be variably represented by the vector sum of the two slips for each subfault. An empirical weighting technique (Yue H et al., 2017) was adopted to determine the relative weighting between SM and SAR observations, and Laplacian smoothing is applied in the inversion.

3. Results

The preferred fault model at strike/dip angles of $350^\circ/76^\circ$ along with its slip distribution is shown in Figure 3. The preferred slip model achieved a variance reduction of 58% and 96% for strong motion and SAR interferometry, respectively (Figure 4). The obtained slip pattern shows a clear upward propagation with peak slip of ~ 0.8 m occurred around 24 km depth and main slip area locates between 15–30 km depth, which is about 10 km above the hypocenter. The total seismic moment is about 1.42×10^{19} N·m, equivalent to a moment magnitude of 6.73, which is close to the moment magnitude obtained from the point source solution. The moment rate function in Figure 1 shows that the slip initiated in the beginning 5 s is small in comparison with the main slips that occurred at deep depths, and the entire rupture process lasts for about 17 s, with the peak moment rate reaching 2.8×10^8 N·m/s about 10 s after the initiation of the mainshock. The centroid time of subfault moment release is plotted as counter lines in Figure 3, which shows the rupture took about 7 s to propagate from the hypocenter to the edge of the main slip area, revealing a low-rupture velocity of about 1 km/s. Then the rupture velocity increases to about 3 km/s for the main slip area, which is close to the rupture velocity of a regular earthquake. Though upward rupture propagation for a reversed faulting is Mode II rupture (Conrad et al., 2003), which may produce super-shear rupture velocity (Xu JK et al., 2015), we did not find evidence supporting a super-shear rupture. The subfault source time function near the hypocenter also shows several peaks, presenting several energy releases. Such phenomena can be interpreted as a “cascaded” slip model (Ellsworth and Beroza, 1995; Yue H et al., 2017; Zhang X et al., 2020), which involves sequential rupture of several asperities, though their detailed slip pattern is beyond the resolution of our slip model.

Aftershocks are mostly located above and beneath the main slipped area. The deeper aftershocks are more active

than the shallower ones and mostly occurred above the fault plane, which is consistent with the dilatation domain produced by a reversed faulting. For earthquake rupture studies conducted in recent years, it is a common strategy to parameterize fault geometry using aftershock distributions. Such practice is more popular for shallow earthquakes, for which the high location precision enables discrimination of events that occurred on the main fault plane or off-fault branches, e.g., Yue H et al. (2017). It is also widely observed that the overall aftershock distribution is not symmetrically distributed around the main fault plane. The dilatational domain enables more intensive aftershock activities, thus introduce a rotation when using all aftershocks to parameterize the fault plane. For the 2018 Hokkaido earthquake, most aftershocks locate above the bottom edge of the co-seismic rupture, which appears to be controlled by the increased Coulomb stress produced by the mainshock faulting (Figure 5). Though the high uncertainty of aftershock locations doesn't enable precisely determine the lineated off-fault structure, it is implied that these events most occur on off-fault structures. We also test parameterizing the fault plane with respect to aftershock locations, which shows such parameterization produces limited improvement to the data fitting (Figures 3 and 5). Considering the complexity of the aftershock triggering mechanism and limited improvement to data fitting, we only rely on the mainshock focal mechanisms to parameterize a single fault plane.

4. Discussion

As a standard model describing the strength of the lithosphere, Burov and Diament (1995) proposed a “sandwich” model to describe the layered strength structure of the continental lithosphere. In this configuration, yielding stress envelop (strength) of rocks is controlled by two competing processes, e.g., “brittle” failure and “ductile” processes. The “brittle” failure process follows the Byerlee’s relationship (Byerlee, 1978), which releases shear stress excess through frictional sliding; thus, the rock strength is controlled by the frictional coefficients. On the one hand, the “ductile” process relies on viscous deformation to release strain loading. The yield strength at a particular depth is thus determined by the minimum strength of two processes, and a typical “sandwich” model is composed of the brittle upper crust and upper mantle, embedded by a ductile lower-crust. We compared the slip model of the 2018 Hokkaido event with the regional velocity models and found this event mostly lies within the ductile regime of the typical “sandwich model”. Zhao DP et al., (1992) applied an inversion method to determine the depth distributions of the Conrad and Moho discontinuities

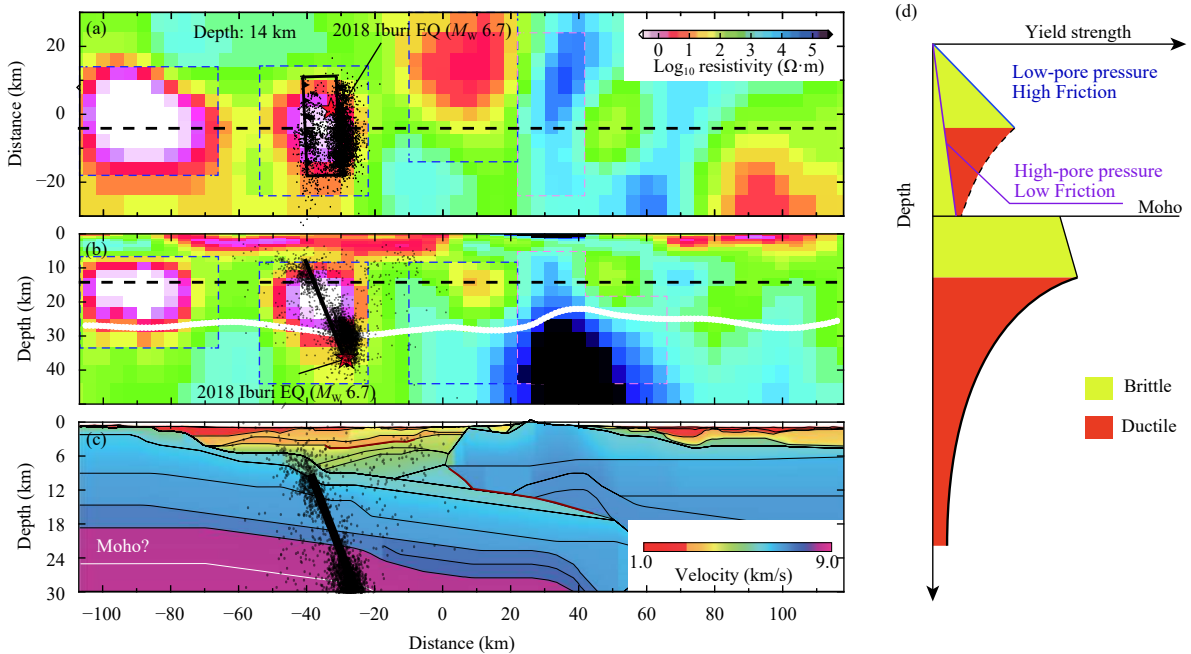


Figure 5. Underground structure and “Sandwich” mode. (a) Mapview of resistivity structure at 14 km depth is plotted in a white to black color scale. Seismogenic area of the $M_w 6.7$ earthquake is marked as dashed box. The mainshock fault plane is plotted as a black box. Epicentral locations of aftershocks are denoted as black dots. The profile of Figure 5b is marked as a black dashed line. (b) Resistivity structure along a depth profile crossing the source area is plotted using the same color scale as Figure 5a. Fault plane and aftershocks are plotted using the same symbol as Figure 5a. White curve shows the depth of the Moho discontinuity. Depth of resistivity distribution in Figure 5a are marked as a black dashed line. (c) Velocity structure along the same depth profile as Figure 5b are plotted in a red-magenta color scale modified from Iwasaki et al. (2019) based on ray-tracing technique. The white line marked the Moho discontinuity, which is shallower than that from JIVSM and Matsubara et al. (2017) model from seismic tomography. (d) “Sandwich” model for yield strength at different depths with brittle filled as yellow and ductile as orange.

beneath the whole of the Japan Islands. Their results show the Moho in the source region is at a depth of ~34 km with a standard error of less than 2 km. Miyamachi et al. (1994) applied an inverse method to P and S wave arrival time data from local earthquakes to estimate a three-dimensional velocity structure beneath northern Japan, and revealed the Moho discontinuity in the source region is about 34 km with a range from ± 2 km to ± 3 km. Katsumata (2010) estimated the depth of the Conrad and Moho discontinuities beneath the Japan Islands using a tomographic inversion of regional body wave arrival times, indicating Moho in the source region is at a depth of 32–34 km with a 0.5–2 km uncertainty. Matsubara et al. (2017) published a digital map of the Moho discontinuity beneath the Japan Islands through three-dimensional seismic tomography, which determines the depth of the discontinuity in the source region is 32–34 km. All these models above are consistent with JIVSM (Koketsu et al., 2012). Iwasaki et al. (2019) imaged lithosphere structures of the Northeast Japan Arc through common reflection surface and multi-dip reflection surfaces method (CRS/MDRS) stacking method raveled the Moho is at depths of 26–28 km in the source region with travel times

at the far offsets containing 0.3–0.5 s ambiguity in proportion to an error about 8 km or less (Figure 5c), replenishing their upper and middle crustal velocity model (Iwasaki et al., 2004). These models reach a consensus that the main slip area is located above the Moho discontinuity and concentrated in the lower crust, which is a typical “ductile” domain in the sandwich model.

On the other hand, shallow depth earthquakes commonly follow the principles of Anderson’s faulting (Anderson, 1951). Presumably, we can consider the vertical axes to be a principal axis in stress tensor since no shear stress is presented at the free-surface. Then shallow depth earthquakes should follow low dip-angle thrust events, high-angle normal events and sub-vertical strike-slip faulting, when the vertical principal stress axis is the maximum, minimum and medium components, respectively. Exceptional events reflect abnormal stress fields, which are related to local tectonic processes, e.g., high-angle reversed faulting of Longmenshan faults produced by detachment structure (Xu Y et al., 2009). The velocity structure of the source area doesn’t reflect a large scale detachment structure at ~30 km scale (Figure 5). If we assume the principle compressional stress is horizontal and

not tilted by the regional tectonic processes, the high dip angle of the 2018 Hokkaido event indicates low-fault friction, thus $\mu \leq \cot(\text{dip}) \approx 0.3$, which is lower than the regular frictional parameter (0.6). Pore-pressure is one typical factor that contributes to weak fault strength, since $(\sigma - p)$ is the effective normal stress applied on fault planes. For example, Coulomb stress calculation for crustal earthquakes generally assumes a frictional parameter of 0.4. Ichihara et al. (2019) proposed a resistivity model (Figure 5a and 5b), which shows a conductive anomaly lies above the hypocenter of the event, which is consistent with the slip area of the Hokkaido event. Low-resistivity is a strong indicator for high-fluid content, thus high pore-pressure, which may explain the abnormally low frictional parameter.

Low-friction also helps to explain the location of major slips in the lower crust. The typical “sandwich” model (Bürgmann and Dresen, 2008) is obtained by assuming a regular frictional coefficient of 0.6 obtained by rock experiments; thus, the brittle to ductile transition is obtained by the intersection of two lines. If the frictional coefficient is smaller, e.g., 0.3 as that proposed by the above stress analysis, the intersection between brittle and ductile strength curves may occur at much deeper depths, Figure 5d, making the whole lower crust depth to be controlled by brittle failure. In summary, the observation of regional seismicity, which includes a seismic nucleation and aftershock concentration in the upper mantle as also a concentration of major slips in the lower crust is consistent with the proposed model of low shear strength.

Another interesting feature of the 2018 Hokkaido earthquake is limited aftershocks are presented at the centroid depth. Complimentary patterns between co-seismic slips and aftershocks are commonly found for modern earthquakes (e.g., Yue H et al. 2014, 2017), in which aftershocks generally distribute surrounding the co-seismic slipped patches. For the 2018 Hokkaido earthquake, such a pattern only exists in the up and bottom edge of the co-seismic ruptures. Based on the joint inversion result, we calculate the co-seismic Coulomb failure stress (CFS) change. In comparison with the receiving mechanism same as the main shock with a dip angle of $\sim 70^\circ$, a conjugate mechanism with a dip angle of $\sim 50^\circ$ is more consistent with the distribution of aftershocks in areas where CFS increases (Figure S7). A dip angle of 50° is also more consistent with the lineation of these down-dip aftershocks. Limited aftershocks occurred between 15–25 km though Coulomb stress is also elevated (Figure S7) on two sides of the slipped area, which indicates aseismic slip dominated stress releasing. Two mechanisms appear to control the stress releasing behavior at the slip concentration depth: unstable sliding controls dynamic rupture producing concentrated slips at this depth;

on the other hand, stable sliding appears to dominate the after-slip period, producing limited seismic activities. Rate and state-dependent friction law (RSF) is commonly adopted to explain seismic versus aseismic slip behaviors using velocity weakening and strengthening mechanisms. A strong patch with efficient dynamic weakening is introduced by Noda and Lapusta (2013) in a numerical simulation study to explain the co-existence of both seismic and aseismic slips at the same fault loci. Such frictional mechanism produces aseismic slip under slow loading and unstable sliding under fast loading, which requires thermal pressurization of pore fluid within and adjacent to the deforming fault core to produce concentrated shear sliding (Rice, 2006, Platt et al., 2014). Thus, high fluid content, as evident in conductivity images, also helps to explain the dynamic weakening feature of the main slipped area. Low-friction properties appear to be not only related to the elevated pore-pressure, but also related to the weakening effect that occurred in dynamic ruptures.

5. Conclusions

We present a kinematic rupture model for the 2018 Hokkaido earthquake, which is jointly inverted from strong motion and InSAR observations. The slip model reveals a deep rupture initiation in the upper mantle and an upward propagation with the majority of slips concentrated in the lower crust. The rupture initiation is characterized by low rupture velocity and low moment release function. Co-seismic slips reveal a complementary pattern with aftershock activities near its the up and bottom edge, which is consistent with co-seismic stress change on conjugate faulting. The abnormally high dip angle, centroid slip location in the lower crust and co-existence of seismic and aseismic behaviors may be reconciled by high fluid pressure.

Acknowledgments

The SM data are recorded by Japan’s KiK- and K-net, download from the website of National Research Institute for Earth Science and Disaster Resilience (NIED). The ALOS-2 SAR observations are accessed from JAXA. Matlab is used for seismic and InSAR data processing and inversion. Digital elevation model (DEM) data from the Shuttle Radar Topography Mission (SRTM) is used for InSAR data processing and map plotting. All figures were drawn using the Generic Mapping Tools. This work is supported by the National Key R&D Program of China (No. 2018YFC1504203) and the National Natural Science Foundation of China (No. 42021003). We thank three anonymous reviewers for their valuable suggestions.

Supplementary Material

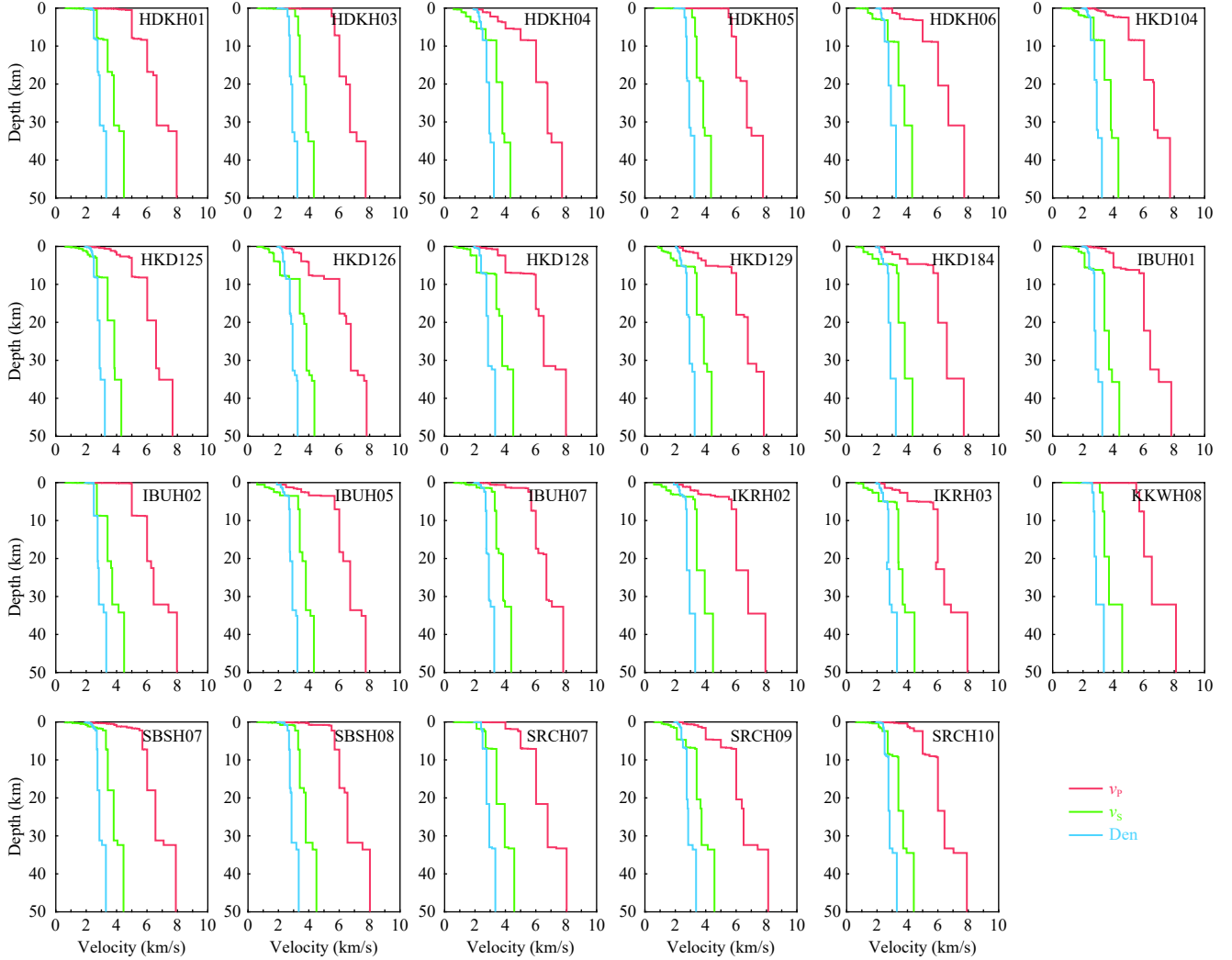


Figure S1. The velocity model below each station extracted from the three-dimensional velocity structure, v_p , v_s and density are marked with red, green and blue, respectively.

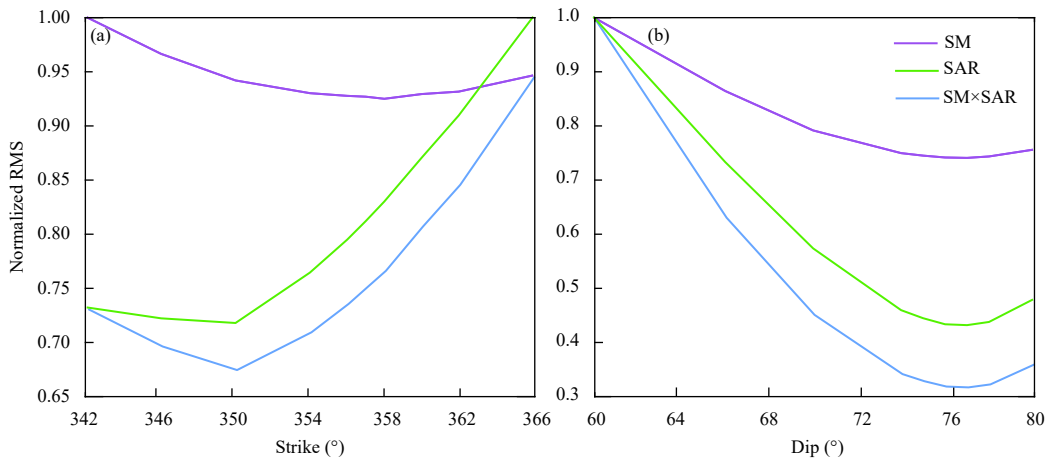


Figure S2. Normalized RMS L-curves of strong motions (SM), synthetic aperture radar (SAR), and SM×SAR for strike (a) and dip angles test (b), marked with purple, green, and blue, respectively. The optimal strike and dip angles for minimum error is 350° and 76° .

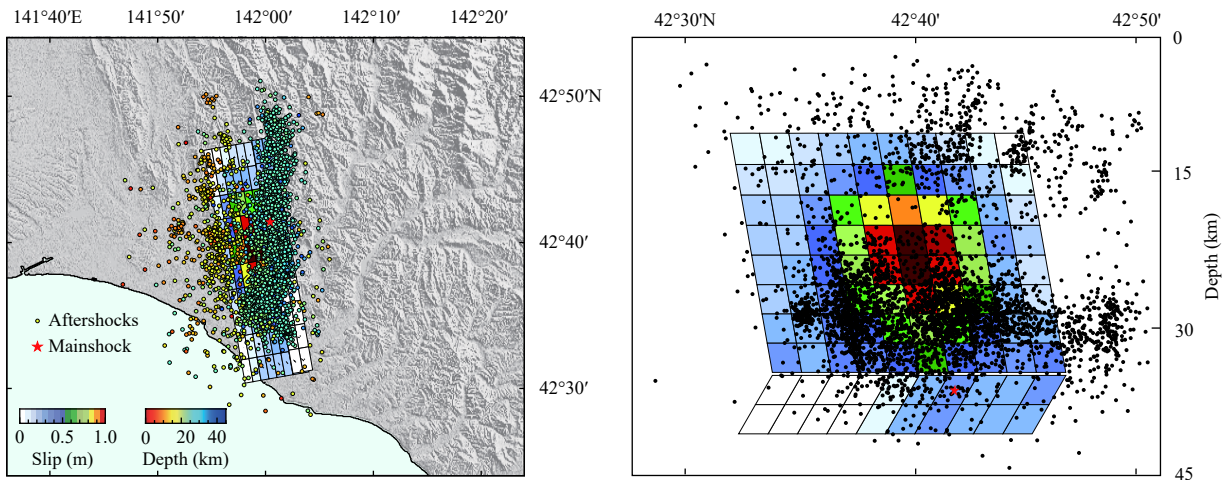


Figure S3. Finite fault model with two segments based on the result of Kobayashi et al., (2019). The major fault plane is east-dipping with a size of 2124 km^2 , strike angle at 350° and dip angle at 70° . Minor one is west-dipping with a size of 216 km^2 , strike at 170° and dip angle at 65° . The element symbols represent the same things as appeared in Figures 1 and 3.

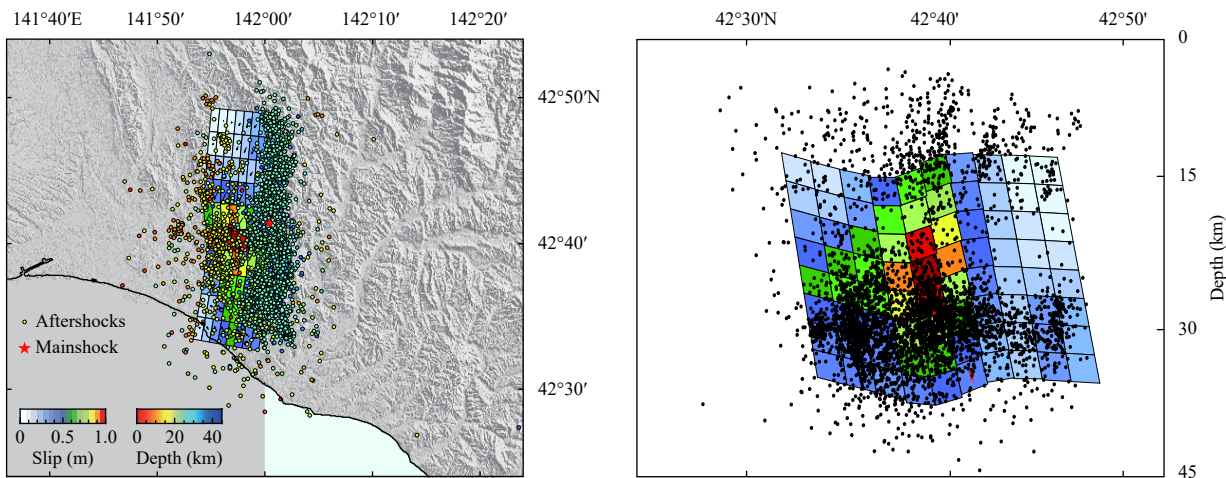


Figure S4. Finite fault model with curved fault plane modified from the result of Asano and Iwata (2019). Also the element symbols represent the same things as appeared in Figures 1 and 3.

Table S1. Fault models from some institutions or researches.

Source	Depth (km)	Centroid depth (km)	Strike ($^\circ$)	Dip ($^\circ$)	Rake ($^\circ$)
USGS	40.5	--	333	61	83
GCMT	35	30.8	349	68	102
JMA	37	33	358	74	113
(Zang C et al., 2019)	37	26	352	70	100
(Asano and Iwata, 2019)	37.04	26	10/355/5 (3 segments)	70	--
(Kobayashi et al., 2019)	41	22	350/170 (2 segments)	70/65	--
(Guo ZL et al., 2019)	--	15.5	347.2	79.6	--
(Kubo et al., 2020)	37.04	25–30	15/–20/40 (curved planes)	65	--
This study	37	25	350	76	--

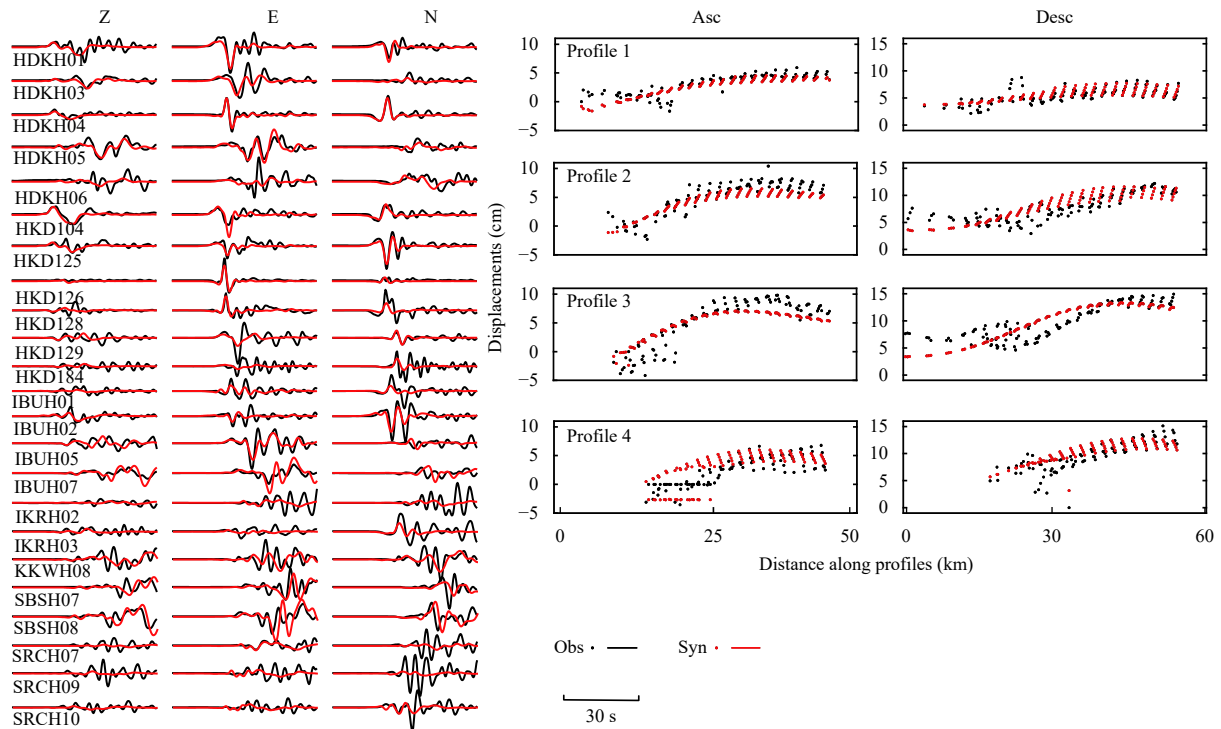


Figure S5. Data fitting for the curved slip model in Figure S3. The profiles are same as Figure 4c and 4d, and the element symbols represent the same things as appeared in Figure 4.

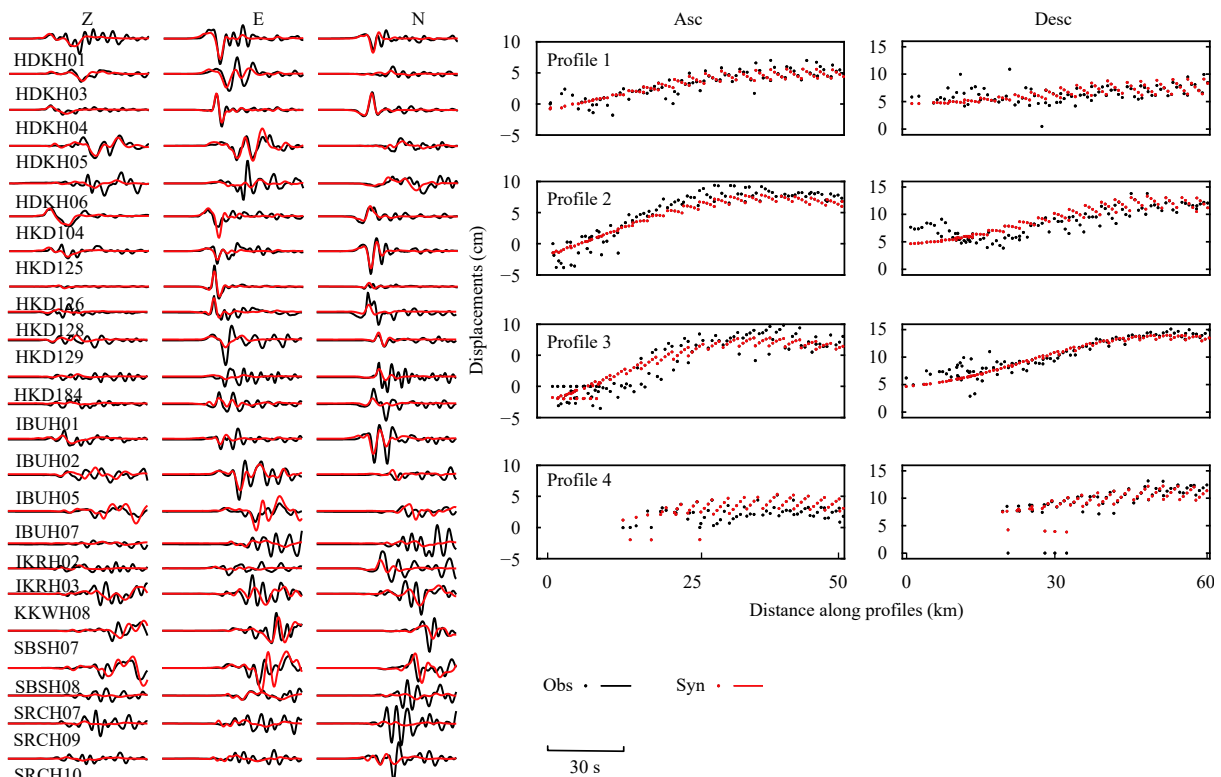


Figure S6. Data fitting for the segmented slip model in Figure S4. The element symbols represent the same things as appeared in Figure 4.

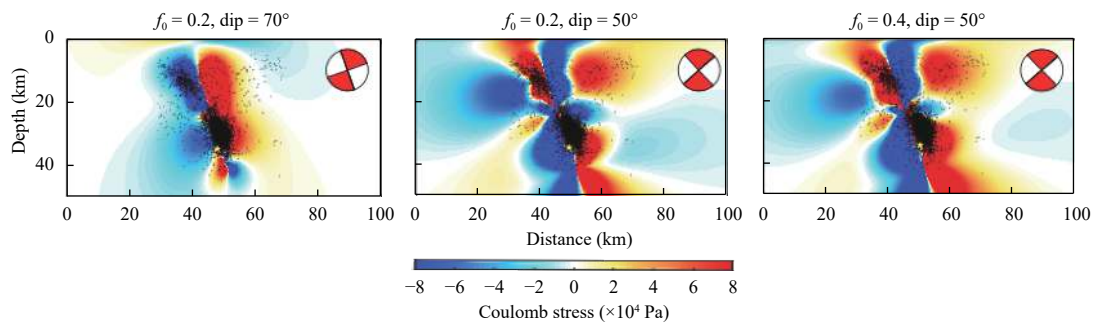


Figure S7. The aftershocks distribution and coulomb stress changes caused by the co-seismic rupture. Red represents an increase in Coulomb stress, and blue is the opposite. The three results correspond to different friction parameters and receiving faults with different dipping angles as plotted at top right corner.

References

- Anderson EM (1951). The dynamics of faulting and Dyke formation with application to Britain, 2nd edn. Oliver and Boyd, Edinburgh, pp.206.
- Arita K, Ikawa T, Ito T, Yamamoto A, Saito M, Nishida Y, Satoh H, Kimura G, Watanabe T, Ikawa T, and Kuroda T (1998). Crustal structure and tectonics of the Hidaka Collision Zone, Hokkaido (Japan), revealed by vibroseis seismic reflection and gravity surveys. *Tectonophysics* **290**(3-4): 197–210.
- Asano K, and Iwata T (2019). Source rupture process of the 2018 Hokkaido Eastern Iburi earthquake deduced from strong-motion data considering seismic wave propagation in three-dimensional velocity structure. *Earth Planets Space* **71**: 101.
- Bürgmann R, and Dresen G (2008). Rheology of the lower crust and upper mantle: Evidence from rock mechanics, geodesy, and field observations. *Ann Rev Earth Planet Sci* **36**: 531–567.
- Burov EB, and Diament M (1995). The effective elastic thickness (T_e) of continental lithosphere: what does it really mean? *J Geophys Res* **100**(B3): 3905–3927.
- Byerlee J (1978). Friction of rocks. *PAGEOPH* **116**(4-5): 615–626.
- Chen CW, and Zebker HA (2001). Two-dimensional phase unwrapping with use of statistical models for cost functions in nonlinear optimization. *J Opt Soc Am A* **18**(2): 338–351.
- Conrad MPC, Smith GD, and Fernlund G (2003). Fracture of solid wood: a review of structure and properties at different length scales. *Wood Fiber Sci* **35**(4): 570–584.
- Demets C (1992). Oblique convergence and deformation along the Kuril and Japan trenches. *J Geophys Res* **97**(B12): 17615–17625.
- Ekström G, Nettles M, and Dziewoński AM (2012). The global CMT project 2004–2010: Centroid-moment tensors for 13,017 earthquakes. *Phys Earth Planet Inter* **200–201**: 1–9.
- Ellsworth WL, and Beroza GC (1995). Seismic evidence for an earthquake nucleation phase. *Science* **268**(5212): 851–855.
- Guo ZL, Wen YM, Xu GY, Wang S, Wang XH, Liu Y, and Xu CJ (2019). Fault slip model of the 2018 M_W 6.6 Hokkaido Eastern Iburi, Japan, earthquake estimated from satellite radar and GPS measurements. *Remote Sens* **11**(14): 1667.
- Hartzell SH, and Heaton TH (1983). Inversion of strong ground motion and teleseismic waveform data for the fault rupture history of the 1979 Imperial Valley, California, earthquake. *Bull Seismol Soc Amer* **73**(6): 1553–1583.
- Hayes GP, Wald DJ, and Johnson RL (2012). Slab1.0: A three-dimensional model of global subduction zone geometries. *J Geophys Res: Solid Earth* **117**(1): B01302.
- Ichihara H, Mogi T, Satoh H, and Yamaya Y (2019). Electrical resistivity modeling around the Hidaka collision zone, Northern Japan: regional structural background of the 2018 Hokkaido Eastern Iburi earthquake (M_W 6.6). *Earth Planets Space* **71**(1): 100.
- Ichikawa M (1971). Reanalyses of mechanism of earthquakes which occurred in and near Japan, and statistical studies on the nodal plane solutions obtained, 1926–1968. *Geophys Mag* **35**: 207–274.
- Ito T (2002). Active faulting, lower crustal delamination and ongoing Hidaka arc-arc collision, Hokkaido, Japan. In: Fujinawa Y, and Yoshida A (eds) *Seismotectonics in Convergent Plate Boundary*, Terra Scientific Publishing Company, Tokyo, pp 219–224.
- Iwasaki T, Adachi K, Moriya T, Miyamachi H, Matsushima T, Miyashita K, Takeda T, Taira T, Yamada T, and Otake K (2004). Upper and middle crustal deformation of an arc-arc collision across Hokkaido, Japan, inferred from seismic refraction/wide-angle reflection experiments. *Tectonophysics* **388**(1-4): 59–73.
- Iwasaki T, Tsumura N, Ito T, Arita K, Makoto M, Sato H, Kurashimo E, Hirata N, Abe S, Noda K, Fujiwara A, Kikuchi S, and Suzuki K (2019). Structural heterogeneity in and around the fold-and-thrust belt of the Hidaka Collision zone, Hokkaido, Japan and its relationship to the aftershock activity of the 2018 Hokkaido Eastern Iburi Earthquake. *Earth Planets Space* **71**: 103.
- Jónsson S, Zebker H, Segall P, and Amelung F (2002). Fault slip

- distribution of the 1999 M_w 7.1 Hector Mine, California, earthquake, estimated from satellite radar and GPS measurements. *Bull Seismol Soc Amer* **92**(4): 1377–1389.
- Katsumata A (2010). Depth of the Moho discontinuity beneath the Japanese islands estimated by traveltime analysis. *J Geophys Res: Solid Earth* **115**(4): B04303.
- Katsumata K, Ichiyanagi M, Ohzono M, Aoyama H, Tanaka R, Takada M, Yamaguchi T, Okada K, Takahashi H, Sakai S, Matsumoto S, Okada T, Matsuzawa T, Hirano S, Terakawa T, Horikawa S, Kosuga M, Katao H, Iio Y, Nagaoka A, Tsumura N, Ueno T, and the Group for the Aftershock Observations of the 2018 Hokkaido Eastern Iburi Earthquake (2019). The 2018 Hokkaido Eastern Iburi earthquake ($M_{JMA} = 6.7$) was triggered by a strike-slip faulting in a stepover segment: insights from the aftershock distribution and the focal mechanism solution of the main shock. *Earth Planets Space* **71**: 53.
- Kimura G (1994). The latest Cretaceous-early Paleogene rapid growth of accretionary complex and exhumation of high pressure series metamorphic rocks in northwestern Pacific margin. *J Geophys Res: Solid Earth* **99**(B11): 22147–22164.
- Kimura G (1996). Collision orogeny at arc-arc junctions in the Japanese Islands. *Island Arc* **5**(3): 262–275.
- Kobayashi H, Koketsu K, and Miyake H (2019a). Rupture process of the 2018 Hokkaido Eastern Iburi earthquake derived from strong motion and geodetic data. *Earth Planets Space* **71**: 63.
- Kobayashi T, Hayashi K, and Yarai H (2019b). Geodetically estimated location and geometry of the fault plane involved in the 2018 Hokkaido Eastern Iburi earthquake. *Earth Planets Space* **71**: 62.
- Koketsu K, Miyake H, and Suzuki H (2012). Japan integrated velocity structure model version 1. The 15th World Conference on Earthquake Engineering, Lisbon, 2012, pp 1–4. http://www.iitk.ac.in/nicee/wcee/article/WCEE2012_1773.pdf.
- Kubo H, Iwaki A, Suzuki W, Aoi S, and Sekiguchi H (2020). Estimation of the source process and forward simulation of long-period ground motion of the 2018 Hokkaido Eastern Iburi, Japan, earthquake. *Earth Planets Space* **72**: 20.
- Lawson CL, and Hanson RJ (1974) Solving least squares problems. Prentice-Hall, Englewood Cliffs, pp 148–157.
- Liu X, Zhao DP, and Li SZ (2013). Seismic heterogeneity and anisotropy of the southern Kuril arc: Insight into megathrust earthquakes. *Geophys J Int* **194**(2): 1069–1090.
- Matsubara M, Sato H, Ishiyama T, and Van Horne A (2017). Configuration of the Moho discontinuity beneath the Japanese Islands derived from three-dimensional seismic tomography. *Tectonophysics* **710–711**: 97–107.
- Miyamachi H, Kasahara M, Suzuki S, Tanaka K, and Hasegawa A (1994). Seismic velocity structure in the crust and upper mantle beneath northern Japan. *J Phys Earth* **42**(4): 269–301.
- Moriya T (1972). Aftershock activity of the Hidaka mountains earthquake of January 21, 1970. *J Seismol Soc* **24**: 287–297 (in Japanese with English abstract).
- Moriya T, Miyamachi H, and Kato S (1983). Spatial distribution and mechanism solutions for foreshocks, mainshock, and aftershocks of the Urakawa-oki earthquake of March 21, 1982. *Geophys Bull Hokkaido Univ* **42**: 191–213 (in Japanese with English abstract).
- Moriya T, Okada H, Matsushima T, Asano S, Yoshii T, and Ikami A (1998). Collision structure in the upper crust beneath the southwestern foot of the Hidaka Mountains, Hokkaido, Japan as derived from explosion seismic observations. *Tectonophysics* **290**(3–4): 181–196.
- Noda H, and Lapusta N (2013). Stable creeping fault segments can become destructive as a result of dynamic weakening. *Nature* **493**(7433): 518–521.
- Platt JD, Rudnicki JW, and Rice JR (2014). Stability and localization of rapid shear in fluid-saturated fault gouge: 2. Localized zone width and strength evolution. *J Geophys Res: Solid Earth* **119**(5): 4334–4359.
- Rice JR (2006). Heating and weakening of faults during earthquake slip. *J Geophys Res: Solid Earth* **111**(B5): B05311.
- Rosen PA, Gurrola E, Sacco GF, and Zebker H (2012). The InSAR scientific computing environment. Proceedings of the European Conference on Synthetic Aperture Radar, Nuremberg, Germany, April 23, 2012, pp 730–733. <https://trs.jpl.nasa.gov/handle/2014/43527>.
- Sakakibara M (1986). A newly discovered high-pressure terrane in eastern Hokkaido, Japan. *J Metamorph Geol* **4**(4): 401–408.
- Shiina T, Takahashi H, Okada T, and Matsuzawa T (2018). Implications of seismic velocity structure at the junction of Kuril-Northeastern Japan arcs on active shallow seismicity and deep low-frequency earthquakes. *J Geophys Res: Solid Earth* **123**(10): 8732–8747.
- Toyoshima T (1989). Tectonic evolution of the Hidaka metamorphic belt and its implication in late Cretaceous-middle Tertiary tectonics of Hokkaido, Japan. Dissertation, Hiroshima University.
- Wang RJ, Lorenzo-Martín F, and Roth F (2006). PSGRN/PSCMP – a new code for calculating co- and post-seismic deformation, geoid and gravity changes based on the viscoelastic-gravitational dislocation theory. *Comput Geosci* **32**(4): 527–541.
- Wells DL, and Coppersmith KJ (1994). New empirical relationships among magnitude, rupture length, rupture width, rupture area, and surface displacement. *Bull Seismol Soc Amer* **84**(4): 974–1002.
- Xu JK, Zhang HM, and Chen XF (2015). Rupture phase diagrams for a planar fault in 3-D full-space and half-space.

- Geophys J Int **202**(3): 2194–2206.
- Xu Y, Huang RQ, Li ZW, Xu Y, Liu JS, and Liu JH (2009). S-wave velocity structure of the Longmen Shan and Wenchuan earthquake area. Chin J Geophys **52**(2): 329–338 (in Chinese with English abstract).
- Yue H, Lay T, Rivera L, An C, Vigny C, Tong XP, and Báez Soto JC (2014). Localized fault slip to the trench in the 2010 Maule, Chile $M_W = 8.8$ earthquake from joint inversion of high-rate GPS, teleseismic body waves, InSAR, campaign GPS, and tsunami observations. J Geophys Res: Solid Earth **119**(10): 7786–7804.
- Yue H, Ross ZE, Liang CR, Michel S, Fattah H, Fielding E, Moore A, Liu Z, and Jia B (2017). The 2016 Kumamoto $M_W = 7.0$ earthquake: A significant event in a fault-volcano system. J Geophys Res: Solid Earth **122**(11): 9166–9183.
- Yue H, Zhang Y, Ge ZX, Wang T, and Zhao L (2020). Resolving rupture processes of great earthquakes: Reviews and perspective from fast response to joint inversion. Sci China Earth Sci **63**(4): 492–511.
- Zang C, Ni SD, and Shen ZC (2019). Rupture directivity analysis of the 2018 Hokkaido Eastern Iburi earthquake and its seismotectonic implication. Seismol Res Lett **90**(6): 2121–2131.
- Zhang X, Feng WP, Du HL, Li L, Wang S, Yi L, and Wang YZ (2020). The 2018 $M_W 7.5$ Papua New Guinea earthquake: a dissipative and cascading rupture process. Geophys Res Lett **47**(17): e2020GL089271.
- Zhao DP, Horiuchi S, and Hasegawa A (1992). Seismic velocity structure of the crust beneath the Japan Islands. Tectonophysics **212**(3-4): 289–301.
- Zhu LP, and Rivera LA (2002). A note on the dynamic and static displacements from a point source in multilayered media. Geophys J Int **148**(3): 619–627.